10-1-1993

Spaceborne radar sensing of precipitation above an ocean surface: Polarization contrast study

Alexander Kostinski
Michigan Technological University

John Kwiatkowski
Michigan Technological University

A. R. Jameson
RJH Scientific, Inc.

Spaceborne Radar Sensing of Precipitation above an Ocean Surface: Polarization Contrast Study

ALEXANDER B. KOSTINSKI AND JOHN M. KWIATKOWSKI

Department of Physics, Michigan Technological University, Houghton, Michigan

A. R. JAMESON

Applied Research Corporation, Landover, Maryland

(Manuscript received 28 May 1992, in final form 23 February 1993)

ABSTRACT

This feasibility study explores the potential benefits of polarization adjustment for spaceborne radar sensing of precipitation. More specifically, the role of the wave polarization in separating or "distinguishing" ocean surface return from the hydrometeor echoes of a "chirped" signal is examined.

To that end, experimental as well as computational data for the polarization scattering matrices of hydrometeors and ocean surfaces are obtained and used to calculate ocean and precipitation "response" to the transmitted pulse for various rain rates and incidence angles. The analysis is restricted to X and C bands, but simulations are performed for several signal-to-noise ratios, rain rates, and ocean surfaces. The problem is further restricted to the monostatic case (same polarizations for transmitter and receiver).

Even when the ocean and hydrometeor echoes are mixed throughout the entire radar resolution volume, the results appear promising. It is found that polarization, which provides the best contrast between rain and ocean returns, varies from almost circular near nadir to elliptical at large off-nadir look angles of incidence (ellipticity of 23° at a 40° incidence angle). Calculations show an order of magnitude improvement in the ratio of the returns when compared with the traditional choice of HH (horizontal transmit and receive polarization). The improvement is largest for the range of angles between 15° and 20° but depends on the assumed rain rate and, in particular, on the ocean surface roughness.

The general method described in this paper can be applied to many problems of radar and lidar meteorology, while the specific results reported here may have relevance for future precipitation measurement missions such as Tropical Rainfall Measuring Mission 2.

1. Introduction

Remote sensing of precipitation can provide data essential for many problems of modern climatology. Even the simplest argument that views the earth's climate as a result of the "equator-to-poles heat engine" shows that the tropical region requires special attention because most of the surface–atmosphere heat exchange occurs there. This is particularly true over the tropical ocean, where the distribution of latent heat is essential to successful predictions of any global weather trends. Yet, there are hardly any weather stations over the region and no systematic observational data. This is the motivation behind such National Aeronautics and Space Administration (NASA) missions as the Tropical Rainfall Measuring Mission (TRMM, Simpson et al. 1988), which will use a spaceborne radar as a main precipitation sensor.

Corresponding author address: Dr. Alexander B. Kostinski, Department of Physics, Michigan Technological University, 1400 Townsend Drive, Houghton, MI 49931-1295.

Indeed, the only way to obtain global rainfall data on a systematic basis seems to be a spaceborne sensor. Infrared and visible sensors, however, do not penetrate clouds. Consequently, inference of rainfall is indirect. On the other hand, radar echo provides a more direct measurement.

Spaceborne radar systems often rely on pulse compression to attain required transmitted power (Meneghini and Kozu 1990; Curlander and McDonough 1991; Doviak and Zrnić 1984). But pulse compression generates range sidelobes along with the main pulse. When such a signal is used to detect precipitation over ocean, these "precursors" detect the ocean surface well ahead of the main pulse and mix with the precipitation returns. It becomes essential, therefore, to find ways of "untangling" the precipitation and surface echoes. Some approaches have already been proposed—for example, waveform analysis (Im and Atlas 1988) of the returned signal—but they are relatively hard to implement, and accuracy and reliability are rather poor. As an alternative, the goal of this paper is to explore the potential of polarization diversity for separating hydrometeor and surface returns. In other

words, we attempt to answer the following question: What should the transmitter and receiver polarizations be in order to distinguish between surface and precipitation returns in some "optimal" fashion?

This search for optimal polarizations must be performed for a variety of conditions—for example, different rain rates and ocean surface roughness values, viewing angles, and signal-to-noise ratios, etc.—in order to evaluate robustness of polarimetric adjustment under different meteorological conditions. Clearly, this is not a trivial task as it involves gathering data on depolarization due to scattering by rough surfaces and by hydrometeors for different look angles. Here we report on a first feasibility study and restrict our analysis to the case of a monostatic radar.

2. Background

To define the polarimetric contrast problem precisely we will briefly review basic definitions and postulates of radar polarimetry (Bringi and Hendry 1990; Kostinski and Boerner 1986; Kostinski et al. 1988). These include the 2D complex vector notation of polarization states as well as the definition and measurement of the scattering matrix, and the antenna voltage equation.

a. Polarization ellipse

Throughout this paper we assume monochromatic waves because the pulse durations involved are typically about a microsecond, and at X-band frequency range of 10 GHz or so each pulse still contains 10^4 waves. The electric-field vector of such a monochromatic transverse plane wave traveling in the z direction of an x, y, z Cartesian coordinate system can be expressed as

$$\mathbb{E}(z,t) = \left[|E_x| \cos\left(\omega t - \frac{2\pi}{\lambda} z + \delta_x\right)\right]\mathbb{x} + \left[|E_y| \cos\left(\omega t - \frac{2\pi}{\lambda} z + \delta_y\right)\right]\mathbb{y}, \quad (1)$$

where ω is the angular frequency, λ is the wavelength, and $\mathbb{x}$, $\mathbb{y}$ are unit vectors in the x and y directions, respectively. In vector form,

$$\mathbb{E}(z,t) = \begin{bmatrix} |E_x| \cos\left(\omega t - \frac{2\pi}{\lambda} z + \delta_x\right) \\ |E_y| \cos\left(\omega t - \frac{2\pi}{\lambda} z + \delta_y\right) \end{bmatrix}.$$

Using complex notation,

$$\mathbb{E}(z,t) = \exp\left[i\left(\omega t - \frac{2\pi}{\lambda} z\right)\right]\begin{pmatrix} |E_x| e^{i\delta_x} \\ |E_y| e^{i\delta_y} \end{pmatrix}.$$

Introducing the *complex amplitude* $E_j = |E_j| e^{i\delta_j}$ for $j = x, y$ and removing the time and space components gives

$$\mathbb{E} = \begin{pmatrix} E_x \\ E_y \end{pmatrix},$$

which is the polarization vector representing the original wave (Azzam and Bashara 1977; Born and Wolf 1980; Bringi and Hendry 1990). Note that E_x and E_y include both magnitude and phase. Factoring out the phase of E_x yields

$$\mathbb{E} = \begin{pmatrix} |E_x| \\ |E_y| e^{i\delta} \end{pmatrix}. \quad (2)$$

The intensity of the wave can be determined from the polarization vector $\mathbb{E}$ simply as $I = |E_x|^2 + |E_y|^2$, but in this study we will use the *normalized* version where $I = 1$; that is,

$$\mathbb{E} = \frac{1}{(|E_x|^2 + |E_y|^2)^{1/2}} \begin{pmatrix} |E_x| \\ |E_y| e^{i\delta} \end{pmatrix}, \quad (3)$$

which is the 2D complex *polarization vector* transmitted by the radar (this vector is called a Jones vector in the optics literature and spinor in quantum mechanics).

Figure 1 depicts a general case of polarization ellipse described by $\mathbb{E}$. Let us now define two parameters that describe completely the polarization of the wave, the ellipticity angle ϵ and tilt τ, which are the "fatness" of the polarization ellipse and tilt of its major axis, respectively. The ellipticity is defined as

$$\epsilon = \tan^{-1}\left(\frac{b}{a}\right), \quad (4)$$

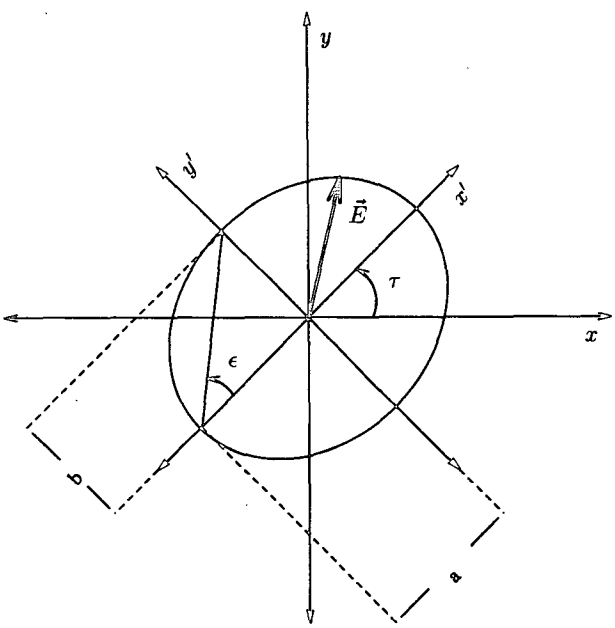

FIG. 1. General case of elliptical polarization of a complex electric-field vector $\mathbb{E}$. Ellipticity ϵ ("fatness" of the ellipse) and tilt τ (inclination of the major axis) are shown.

where b and a are the semiminor and semimajor axes of the ellipse. The sign of ϵ determines the sense of rotation of $\mathbf{E}$, that is, *right-* or *left*-handed polarizations. The ϵ and τ parameters have ranges of $-\pi/4 \leq \epsilon \leq \pi/4$ and $-\pi/2 \leq \tau \leq \pi/2$, respectively. They completely as well as uniquely describe all possible polarizations.

Note that complex conjugation of the polarization vector reverses the sense of rotation of the corresponding polarization ellipse. Also observe that tilt is not defined for circular polarizations. A polarization vector of unit intensity describing a general elliptical polarization can be expressed in terms of ϵ and τ as follows (Azzam and Bashara 1977):

$$\mathbf{E} = \begin{pmatrix} \cos\tau\cos\epsilon - i\sin\tau\sin\epsilon \\ \sin\tau\cos\epsilon + i\cos\tau\sin\epsilon \end{pmatrix}, \tag{5}$$

which is the form used in the calculations throughout the rest of this paper.

b. Scattering matrix

When a polarized wave is scattered by a target, the interaction can be described by a 2×2 complex scattering matrix acting on 2D complex polarization vectors defined by (5)—see, for instance, Bringi and Hendry (1990) and Azzam and Bashara (1977). Note that the $\exp(ikr)/r$ dependence is not included in the definition and the scattering matrix can be regarded as a generalization of a radar cross section. Thus, the scattering matrices of both hydrometeors and the ocean surface can be written as

$$\mathbf{S} = \begin{pmatrix} \mathrm{HH}e^{i\delta_{\mathrm{HH}}} & \mathrm{HV}e^{i\delta_{\mathrm{HV}}} \\ \mathrm{VH}e^{i\delta_{\mathrm{VH}}} & \mathrm{VV}e^{i\delta_{\mathrm{VV}}} \end{pmatrix},$$

where HH, HV, VH, VV are all real quantities that represent the polarizations used to measure the matrix; that is, HH denotes horizontal transmit and receive magnitude (Bohren and Huffman 1983; Ulaby and Elachi 1990), and δ's with subscripts denote the corresponding polarization phases.

The matrix is usually normalized by the (1,1) element to give

$$\mathbf{S} = \mathrm{HH}e^{i\delta_{\mathrm{HH}}} \begin{bmatrix} 1 & \dfrac{\mathrm{HV}}{\mathrm{HH}} e^{i(\delta_{\mathrm{HV}} - \delta_{\mathrm{HH}})} \\ \dfrac{\mathrm{VH}}{\mathrm{HH}} e^{i(\delta_{\mathrm{VH}} - \delta_{\mathrm{HH}})} & \dfrac{\mathrm{VV}}{\mathrm{HH}} e^{i(\delta_{\mathrm{VV}} - \delta_{\mathrm{HH}})} \end{bmatrix}. \tag{6}$$

The overall phase δ_{HH} is not a measurable in our case and can be set to zero.

c. The voltage equation

Given the preceding definition, the polarization of a scattered wave is calculated from the transmitted signal according to the equation

$$\mathbf{E}_s = \mathbf{S}\mathbf{E}_t,$$

where the subscripts t and s denote the transmitted and scattered wave, respectively. The scattering matrix $\mathbf{S}$ contains all the information about the depolarization properties of the target. The scattered wave is then received by the antenna and the *complex* voltage measured at the receiving antenna terminal is given by (Ishimaru 1991, 504–507)

$$V = \mathbf{E}_r^{\mathrm{T}}\mathbf{E}_s = \mathbf{E}_r^{\mathrm{T}}\mathbf{S}\mathbf{E}_t. \tag{7}$$

The subscript r denotes the receiver polarization state and the superscript T denotes the transpose of the polarization vector. Note that $\mathbf{E}_r$ is defined as the polarization vector of the receiving antenna when it is transmitting in the direction of $\mathbf{E}_s$ (Ishimaru 1991; Kostinski and Boerner 1986).

In the case of a monostatic radar considered in this paper, the polarizations of the transmitter and receiver are identical ($\mathbf{E}_r = \mathbf{E}_t$). Therefore (7) reduces to

$$V = \mathbf{E}^{\mathrm{T}}\mathbf{S}\mathbf{E}. \tag{8}$$

3. Problem description

In this section we describe the general situation considered—for example, transmitter–scatterer geometry as well as the relevant physical parameters such as the ocean surface roughness, etc. We then go on to nondimensionalize the problem so that ocean and rain scattering matrix data from different sources can be combined. Next, the criteria for evaluating the spaceborne radar system performance are discussed, and we conclude the section with the mathematical statement of the problem.

a. Scenario

Imagine a spaceborne radar transmitting pulses backscattered by hydrometeors and by the underlying ocean surface as shown in Fig. 2. The rain is assumed to be spatially homogeneous throughout the beam. As

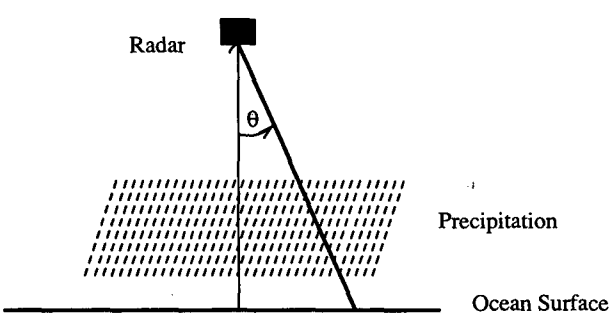

FIG. 2. Geometry of the problem. Spaceborne radar transmits waves at an angle θ with respect to nadir. Propagation path through uniform precipitation is assumed to be 4 km for all incidence angles for simplicity.

discussed in the Introduction, pulse compression is used because of spaceborne radar power limitations.

Consequently, range sidelobes appear. This causes mixing of the two returns at the point of arrival. We then want to study the dependence of the relative strength of the rain and ocean echoes on the transmitted polarization. In other words: Is there an "optimal polarization" for which the hydrometeors are seen "best" against the ocean surface background?

The foregoing question is well defined only when the ocean surface and raindrops are characterized in terms of their scattering matrices; that is, surface roughness and rain rate as well as the angle of incidence are specified. Thus, to combine rain and ocean data from different sources we nondimensionalize the problem so that only relative quantities enter the calculations.

b. *Nondimensionalized model*

For the rest of the paper we imagine the radar to be at a fixed altitude but the look angle as well as the rain rate and ocean roughness are allowed to vary. Then the total (complex) voltage V_t at the receiving antenna is the sum of voltages from rain V_r and ocean V_o returns and an additive Gaussian system noise $\sqrt{\sigma}$ (Meneghini and Kozu 1990). This can be written as

$$V_t = V_r + V_o + \sqrt{\sigma}. \tag{9}$$

On the other hand, the received complex voltage from each scatterer in terms of a scattering matrix is given by

$$V_i = \mathbb{E}_r^{\mathrm{T}} \mathbb{S}_i \mathbb{E}_t, \quad \text{where} \quad i = r, o.$$

For a monostatic arrangement considered here, $\mathbb{E}_r = \mathbb{E}_t$, and the total complex voltage at the antenna can be written as

$$V_t = (\mathrm{HH}_r)\mathbb{E}^{\mathrm{T}}\mathbb{S}_r\mathbb{E} + (\mathrm{HH}_o)\mathbb{E}^{\mathrm{T}}\mathbb{S}_o\mathbb{E} + \sqrt{\sigma}, \tag{10}$$

where the scattering matrices are normalized by their respective HH elements (see end of section 2b).

Our next task is to nondimensionalize (10) so that only the relative strength of the two returns appears in the calculations. To that end let us divide (10) through by HH_r. This yields

$$\frac{V_t}{\mathrm{HH}_r} = \mathbb{E}^{\mathrm{T}}\mathbb{S}_r\mathbb{E} + \left(\frac{\mathrm{HH}_o}{\mathrm{HH}_r}\right)\mathbb{E}^{\mathrm{T}}\mathbb{S}_o\mathbb{E} + \frac{\sqrt{\sigma}}{\mathrm{HH}_r}.$$

We now define $\sqrt{A} \equiv \mathrm{HH}_o/\mathrm{HH}_r$ so that A is the ratio of ocean backscattered power to that of the hydrometeors. Note that A depends on the angle of incidence as well as on the rain rate (Meneghini and Kozu 1990, p. 32).

The total dimensionless received power $P = |V|^2$ can then be written as

$$P_{\text{total}} \equiv \frac{|V_t|^2}{\mathrm{HH}_r^2} = |\mathbb{E}^{\mathrm{T}}\mathbb{S}_r\mathbb{E}|^2 + A|\mathbb{E}^{\mathrm{T}}\mathbb{S}_o\mathbb{E}|^2 + \frac{\sigma}{\mathrm{HH}_r^2}, \tag{11}$$

or in shorthand

$$P_t = P_r + AP_o + P_n,$$

which gives the power P_t in terms of ocean and rain returns, and system noise. Note that incoherent pulse averaging is assumed here over time scales well above rain decorrelation times so that there are no interference terms, and squared voltages add (Meneghini and Kozu 1990, p. 52).

c. *Figure of merit*

Our task is to define what is meant by the best "polarimetric contrast"; that is, we need a "figure of merit" to characterize the performance of the system for different polarizations. A natural quantity to consider as a measure of contrast is the ratio of the rain to ocean return voltages denoted as X (Kostinski and Boerner 1987) and defined as

$$X \equiv \frac{\mathbb{E}^{\mathrm{T}}\mathbb{S}_r\mathbb{E}}{\mathbb{E}^{\mathrm{T}}\mathbb{S}_o\mathbb{E}} = \frac{V_r}{V_o}. \tag{12}$$

However, this ratio is not always a good performance criterion, because it fails to take into account system noise. Indeed, it approaches infinity as the radar polarization approaches such $\mathbb{E}$, which renders the ocean return zero. In fact, a closed form expression for such $\mathbb{E}$ as a function of scattering matrix elements can be obtained (see appendix A for details). Another dissatisfying feature of (12) as a possible figure of merit is the fact that while it can always be made infinite, no weight is given to the actual strength of the rain echo at a given polarization. Indeed, in spite of very large X the rain echo can be so small as to make it totally undetectable for realistic spaceborne radar systems. To remedy this situation we propose a somewhat different quantity—the fractional strength of the rain return compared with the total received power. It is denoted as $\aleph$ and defined as follows:

$$\aleph \equiv \frac{P_r}{P_r + AP_o + P_n}, \tag{13}$$

where P_r, P_o, and P_n are powers (squares of complex voltages) due to rain, ocean surface, and noise, respectively, and are defined by (10) and (11). Thus $\aleph$ gives the strength of the rain signal relative to the total power received as a function of transmit–receive polarization. For small values of P_n and large A (conditions valid near nadir where surface return is much larger than the one due to hydrometeors), $\aleph$ approaches P_r/P_o (see appendix B).

d. Formal problem statement

With the help of (11) and (13) we can now state the problem of polarimetric contrast more precisely. Namely, we wish to find such a transmit–receive polarization **E** for which $\aleph$ is maximal. Such an optimal polarization depends on the magnitudes and phases of the ocean and rain scattering matrix elements as well as on A, all of which are to be obtained from experimental or computational data. These parameters are, in turn, functions of five basic variables: rain rate R, angle of incidence θ (measured from nadir throughout this paper), ocean surface roughness ξ, pathlength of propagation through the precipitation l, and wavelength λ of the incident radiation. In other words, the program of "exploring the potential benefits of polarization diversity" can now be stated as follows: *Given measured or computed scattering matrices of hydrometeors and of the ocean surface as well as system's minimal detectable signal level, find such antenna polarization for which the figure of merit $\aleph$ is maximal. Explore the behavior of such polarizations as well as improvement in $\aleph$ they offer over traditional choices (HH, VV, etc.) as a function of the rain rate R, the incidence angle θ, and the system noise σ.*

4. Data

Our last task before calculating the polarization contrast is to obtain the scattering matrix data to insert in (11). One key parameter is the wavelength λ of the interrogating wave. In this paper we consider only C- and X-band data and calculations. The latter shows most promise in spaceborne applications (13.8 GHz is planned for TRMM) (Meneghini and Kozu 1990). Thus, all of the scattering matrix data are to be obtained for λ of about 5 cm (6 GHz, C band) and 3 cm (10 GHz, X band). Furthermore, these rain and ocean data must be obtained for different values of ocean surface roughness, look angle, and rain rate so that we can study effects of polarization adjustment under diverse meteorological conditions.

The data enters the model as a set of nondimensional quantities (section 3b) except for the propagation phase shift, which has units of inverse length. For this study it is assumed that the one-way pathlength is 4 km; that is, the radar is looking at a range gate located 4 km below the top of the precipitation and just above the ocean surface.

Finally, let us address the following question: Why should random targets such as rain and the ocean surface be modeled by deterministic scattering matrices? Indeed, echoes from such targets fluctuate randomly (e.g., Rayleigh distribution) in time and space. It turns out, however, that these fluctuations often occur "in unison" so that random matrices have a "typical or average" structure. This is much like natural light passed through a polarizer with stochastic amplitude but deterministic polarization. It is the systematic difference in rain and ocean average matrices that this paper attempts to exploit. Similar arguments are behind applications of polarimetry in weather radar. In appendix C we provide experimental justification of this view for the ocean surface scattering.

a. Scattering by the hydrometeors

As described in section 2b, the rain scattering matrices are of the form given in (6). Let us next consider the relative phases. These consist of two contributions: backscattering from a given radar resolution volume, and propagation phases. The relative propagation phase shift between the horizontal and vertical copolarizations is given by twice the pathlength times the rate (with distance) of the propagation differential phase shift Φ (Jameson 1991). At the frequencies considered in this work, the propagation cross-pol phase shift is simply one-half that of a copol. Indeed, propagation effects are cumulative in both directions, and since in cross-pol terms each polarization traverses only half the trip of the copolar return, we have the following relations:

$$\Phi_{HH} = \Phi_H + \Phi_H = 2\Phi_H,$$

$$\Phi_{VV} = \Phi_V + \Phi_V = 2\Phi_V,$$

$$\Phi_{HV} = \Phi_H + \Phi_V,$$

where one subscript is used to denote the one-way propagation phase shift for H or V polarizations and the double subscript denotes the two-way path. The propagation phase shift that a horizontal–vertical transmit–receive system would measure is

$$\Phi_{HV} = \frac{1}{2}(\Phi_{VV} + \Phi_{HH}).$$

The phase *relative to* HH for the cross-pol element is then given by

$$\Phi_{HV} - \Phi_{HH} = \frac{1}{2}(\Phi_{VV} - \Phi_{HH}).$$

The preceding argument holds only in so far as the backscatter phase is negligible compared with the propagation phase. This is valid for frequencies and pathlengths considered here. Note that the propagation phase shift can differ from zero significantly (Jameson 1987). Thus one can write the rain scattering matrix as

$$\mathbf{S}_r = \begin{pmatrix} 1 & \gamma e^{i\phi/2} \\ \gamma e^{i\phi/2} & \beta e^{i\phi} \end{pmatrix},$$

where $\beta \equiv \mathrm{VV}/\mathrm{HH}$ is the ratio of VV to HH returns backscattered off the raindrops and is fairly close to unity near nadir or for moderate rain rates. The off-diagonal matrix term γ denotes the "cross-polarized" power ratio (relative to the HH return power). The cross-polarized rain returns (LDRs) are small compared to β with γ seldom exceeding 10% of the copolar

return. The phase ϕ in the rain matrix is the total differential phase shift, that is, the sum of the differential backscatter phase and the two-way differential propagation phase shift.

Rain calculations described next were used to obtain β versus θ (incidence angle) curves and are shown in Figs. 3 and 4 for C and X bands, respectively. There are seven rain rates ranging from 5.3 to 180.8 mm h^{-1} and nine angles from nadir to 40°. A plot of ϕ versus incidence angle for X band is shown in Fig. 5.

The data for Figs. 3, 4, and 5 were computed as follows. Root-mean-square values of the magnitudes of the backscatter matrix elements in rain were computed for horizontal and vertical copolarizations as well as for their respective cross polarizations. It is assumed that most of the raindrops are quiescent and are *equilibrium shaped;* that is, their shapes are determined by the balance between surface tension, gravity, and aerodynamic forces (Chuang and Beard 1991). These shapes are well approximated as oblates with axis ratios linearly related to the drop size (Pruppacher and Beard 1970):

$$r = 1.03 - 0.62D, \quad D \geq 0.1 \text{ cm}. \tag{14}$$

While drops are highly oriented with vertical axes of symmetry, some do oscillate probably due to collisions with other drops (Beard et al. 1983). The details of such oscillations are not understood, but some of the effects can be represented as a three-dimensional Gaussian distribution of angles (canting angles) between the vertical and the symmetry axes having a zero mean and standard deviation σ_a. Based upon observations, $\sigma_a = 4°$ in these calculations. Rain consists of drops of different sizes. In this study the drop size distributions are assumed to be exponential of the form

$$N(D) = N_0 e^{-\Delta D}, \tag{15}$$

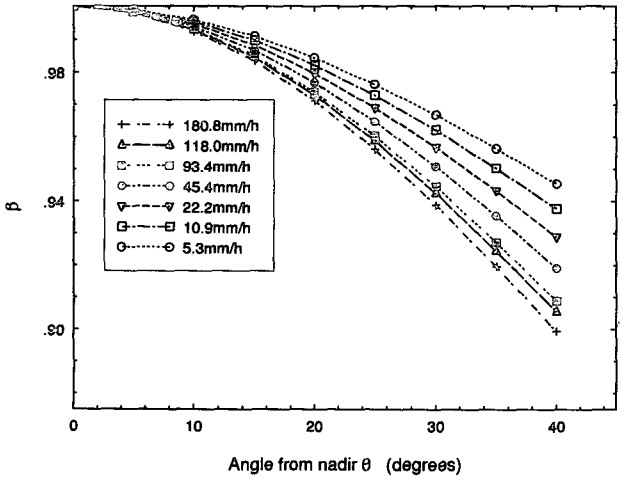

FIG. 3. Ratio of copolar rain returns $\beta \equiv |VV/HH|$ is shown as a function of the incidence angle θ. These computations were performed for C band.

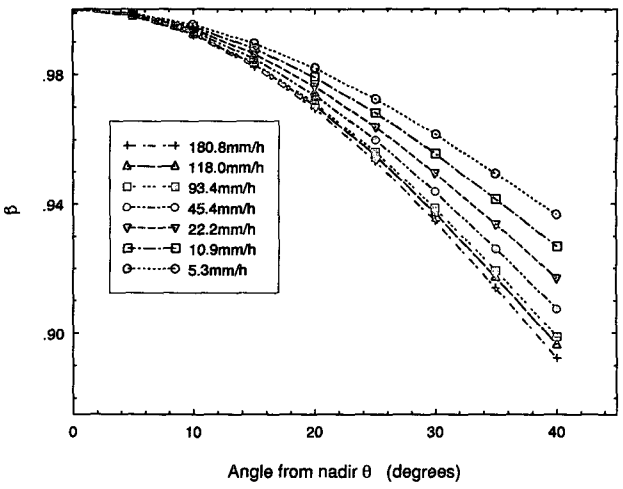

FIG. 4. Ratio of copolar rain returns $\beta \equiv |VV/HH|$ is shown as a function of the incidence angle θ. These computations were performed for X band.

with minimum and maximum drop sizes of 0.01 and 0.60 cm, respectively. Numerous investigations have shown that the parameters Δ (cm^{-1}) and N_0 (cm^{-4}) vary as a function of rainfall rate as well as the type of rain clouds. For a spaceborne radar, the most detectable rain clouds will be thunderstorms. Sekhon and Srivastava (1971) found that in thunderstorms

$$\Delta = 38R^{-0.14}, N_0 = 0.07R^{0.37}, \tag{16}$$

where R is the rainfall rate (mm h^{-1}). These relations are used here to specify the drop size distributions over a range of rainfall rates from 5 to nearly 200 mm h^{-1}.

The ensemble rms average magnitudes of the matrix elements are computed over the entire ensemble of

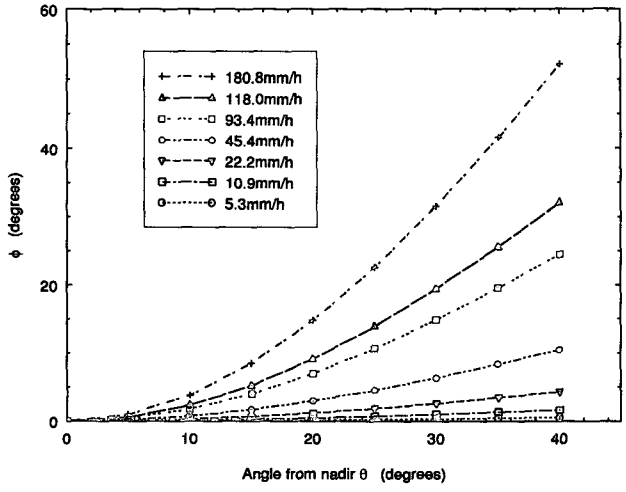

FIG. 5. Total differential phase shift for rain ϕ (combined effect of backscatter and propagation) is shown as a function of incidence angle θ for a 4-km one-way propagation path. These computations were performed for X band.

raindrops by adding the squared magnitudes of the matrix elements calculated for each drop using the Waterman T-matrix solution to the scattering equations for oblate spheroids as modified by Warner and Hizal (1976). The raindrops are essentially Rayleigh–Gans scatterers. Consequently, the viewing geometry can be treated with sufficient accuracy in terms of projected dipole moments (Jameson 1987).

b. Scattering matrices for the ocean surface

The ocean surface return portion of the total power in (11) is characterized by the scattering matrix

$$\mathbf{S}_o = \begin{pmatrix} 1 & \delta e^{i\phi/2} \\ \delta e^{i\phi/2} & \alpha e^{i\phi} \end{pmatrix},$$

where α and δ are real quantities. The cross-pol terms δ are typically less then 10% of α = VV/HH, and α is usually greater than unity. The phase ϕ is the propagation phase shift due to the precipitation medium (it can be seen from the JPL SAR data that differential phase shifts due to backscatter from the ocean surface are negligible at our wavelengths). While the phase contributions from the rain are included in the subsequent simulations, it is shown later that their effects are small. For now it is sufficient to discuss the ocean scattering in the absence of rain.

When propagation effects are neglected, the ocean matrix reduces to

$$\mathbf{S}_o = \begin{pmatrix} 1 & \delta \\ \delta & \alpha \end{pmatrix}.$$

We have been able to find only one set of experimental data in the desired range of wavelengths that contains

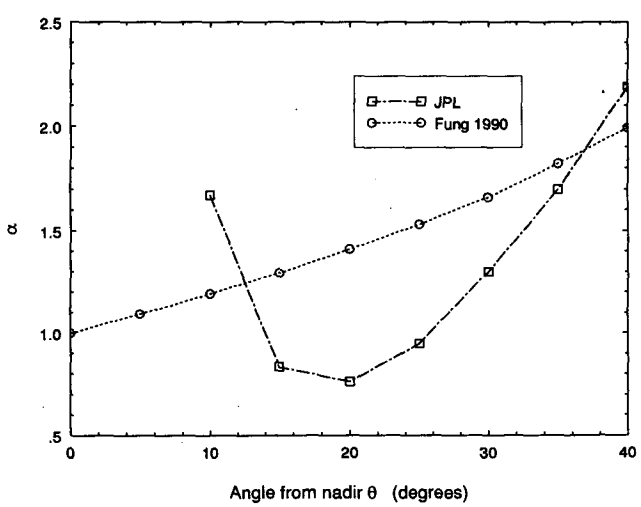

FIG. 6. Ratio of copolar ocean returns $\alpha \equiv |VV/HH|$ is shown as a function of the incidence angle θ. These experimental data and computations were obtained from (Jet Propulsion Laboratory 1991; Fung et al. 1990), respectively.

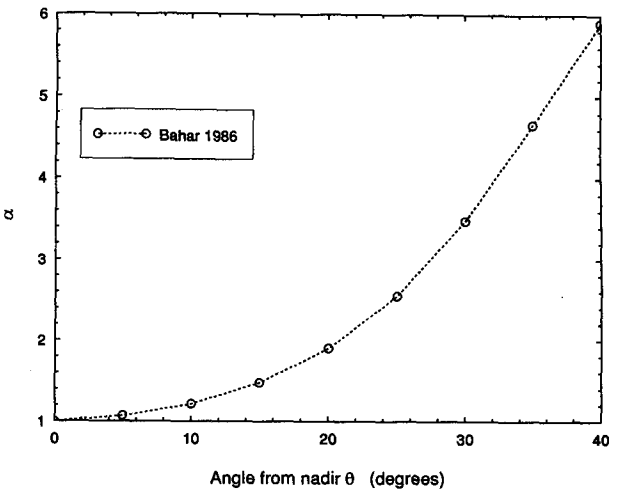

FIG. 7. Ratio of copolar ocean returns $\alpha \equiv |VV/HH|$ is shown as a function of the incidence angle θ. The data for this graph was obtained from computations of Bahar and Fitzwater (1986) and scaled appropriately for X band.

complete polarimetric scattering matrix information. This data was collected by the Jet Propulsion Laboratory (JPL) Synthetic Aperture Radar (SAR) team (Jet Propulsion Laboratory 1991). It contains C-band polarization scattering matrix elements given as functions of the incidence angle (Zebker et al. 1987; Ulaby and Elachi 1990). The dependence of α on the incidence angle is one of the two curves shown in Fig. 6.

Note that while for very rough surfaces and for close-to-nadir look angles the ratio α = VV/HH may drop below unity (Daley 1973; Long 1975). For most ocean surfaces α is greater than unity; that is, HH $\leq$ VV for all angles. For the JPL dataset α is slightly less than unity for look angles between 15° and 25° in Fig. 6.

Also, there are no data for angles ($\leq$10°) and there seems to be no trend toward α = 1 at small angles, which is somewhat disturbing because such behavior affects the maximum of $\aleph$ significantly as we shall see in the next section (see also appendix A).

In view of these atypical features we have decided to supplement this data with another computational set. It is based on the integral equation model approach (Fung et al. 1990) and can be applied to any radar wavelength. However, it is valid only for a relatively smooth surface. At C band the average rms surface height h_{rms} is on the order of 1 cm. The dependence of α on the angle of incidence is also shown in Fig. 6. We see that the dependence is monotonic and in general "better behaved" than the JPL data.

To get some data in the most important case of X band we have included another set based on the unified full-wave approach (Bahar and Fitzwater 1986) and applicable to a relatively rough surface (h_{rms} = 414 cm). The dependence of α on the angle of incidence for this set is shown in Fig. 7.

c. Data for the surface-to-rain ratio

To complete the input data for (11) and (13) we need the ratio of rain-to-ocean return powers A as a function of incidence angle and rain rate. This data was obtained by digitizing a graph from page 32 of Meneghini and Kozu (1990), where A was given as a function angle for various rain rates. The curves were extrapolated to include all the rain rates in this study. The experimental data for A was available only at 13.9 GHz, which differs somewhat from the 9.35-GHz rain calculations. Note that A decreases rapidly with increasing angle θ. For a rain rate of 5 mm h^{-1} A takes on values of 45 to 3 dB for angles from 0° to 40°.

5. Computational procedure

We are now in a position to search for a maximum of $\aleph$ as a function of transmitted polarization. To do this we simply insert the ocean and rain scattering matrix data into (11) to compute voltages and then calculate $\aleph$ according to (13).

To this end, a transmitted polarization vector of unit amplitude as a function of ϵ and τ is constructed as follows (5):

$$\begin{pmatrix} \cos\tau\cos\epsilon - i\sin\tau\sin\epsilon \\ \sin\tau\cos\epsilon + i\cos\tau\sin\epsilon \end{pmatrix}.$$

To determine the polarization response of the scattering system we discretize polarization space by introducing a grid in both ϵ and τ directions (typically 100×200 points, respectively). Such a grid corresponds to a radar with a polarization purity of about a percent.

For each value of ϵ and τ, a transmitted polarization vector is calculated, and the voltage equation (8) is used to determine the complex voltages V_r and V_o at the receiving antenna. The individual powers are calculated next and a value for $\aleph$ is obtained for every point on the grid (e.g., see Fig. 8). The maximum of $\aleph$ is found by a brute force search along with the corresponding polarization coordinates defined as ϵ_{op} and τ_{op}, which in turn define the optimal transmit–receive polarization.

To characterize the improvement provided by polarization adjustment we introduce an improvement factor (IF) defined as

$$\mathrm{IF} \equiv \frac{\aleph_{\max}}{\aleph_{HH}}, \tag{17}$$

where HH polarization is chosen for comparison because it is often used in spaceborne radar applications (Meneghini and Kozu 1990, p. 120; Okamoto et al. 1988, p. 217).

Numerical example. A numerical example of $\aleph$ and the improvement factor IF computations is provided here. The polarization space is divided up into a grid

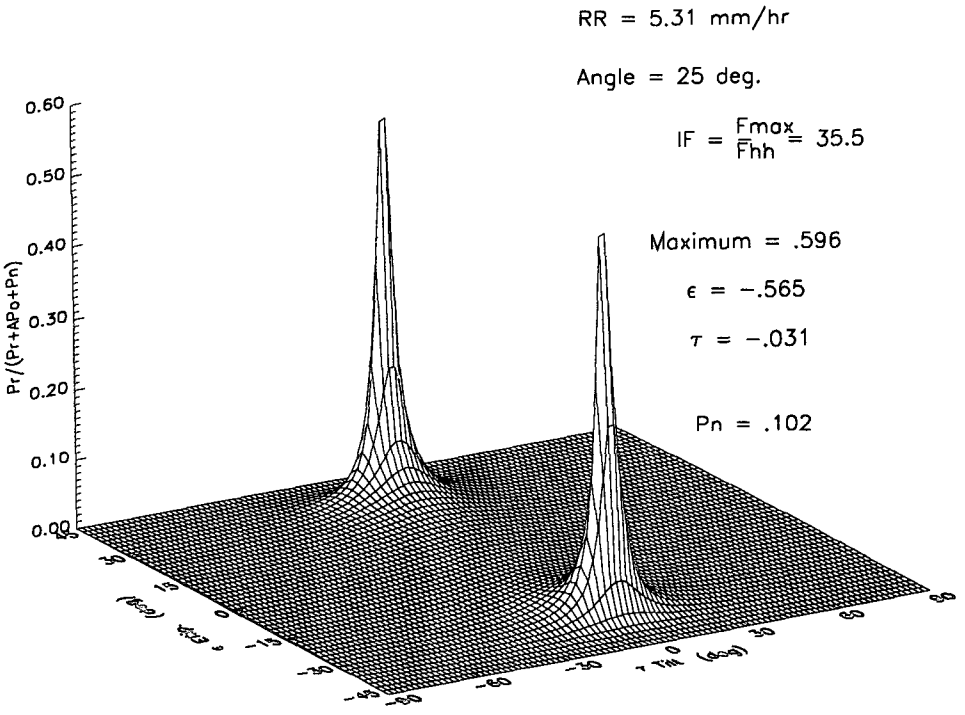

FIG. 8. The figure of merit $\aleph$ (relative strength of rain echo compared with total return) is shown as a function of ellipticity ϵ and tilt τ of the transmitted wave. The computations were performed for a rain rate $R = 5.3$ mm h^{-1} and an angle of incidence θ of 25°.

in ϵ and τ directions. The complex voltages are then evaluated for each ϵ and τ by means of (8). The results (for both ocean and rain) can be expressed as functions $V_o(\epsilon, \tau)$ and $V_r(\epsilon, \tau)$. The powers P_o and P_r can then be calculated and $\aleph$ computed for each ϵ and τ.

To perform the foregoing sequence of calculations we need to construct a polarization vector and obtain the rain and ocean scattering matrices. In the example below a rain rate of 5.3 mm h^{-1} is used and the radar is looking at an angle of 25° off nadir. The wavelength λ = 3.21 cm (X band, 9.35 GHz) so that the ocean data from Bahar and Fitzwater (1986) can be used. There is a slight discrepancy between our rain and ocean data as they are computed for λ's of 3.21 and 3.37 cm, respectively. This could not be avoided because the calculations involve piecing the data from three different sources together. However, the ocean data from (Bahar and Fitzwater 1986) scales with the ratio of wavelength to rms surface height and can therefore be applied exactly as is for an ocean surface of slightly different roughness.

With these parameters the scattering matrices are

$$\mathbf{S}_r = \begin{pmatrix} 1.000 + 0.0i & 0.00532 + 1.15 \times 10^{-5}i \\ 0.00532 + 1.15 \times 10^{-5}i & 0.972 - 0.00419i \end{pmatrix}$$

and

$$\mathbf{S}_o = \begin{pmatrix} 1.000 + 0.0i & 0.0482 + 0.01i \\ 0.0482 + 0.0i & 2.55 + 0.0i \end{pmatrix}.$$

The magnitudes and phases have been resolved into real and imaginary parts, and in both matrices the off-diagonal terms are less then 0.2% of the VV/HH magnitude. For this example the other parameters in the model are

$$A = 58.5, \quad P_n = \frac{\sigma}{\mathrm{HH}_r^2} = 0.102,$$

where σ has been chosen to be numerically equal to HH^2 at the rain rate of 1 mm h^{-1}. This choice corresponds to 1 mm h^{-1} being a minimal detectable rain intensity per pulse. For comparison, NASA's TRMM design allows for 0.5 mm h^{-1} per minimal detectable intensity (Meneghini and Kozu 1990).

Let us now pick a transmitted polarization defined by $\epsilon = -0.565$ and $\tau = -0.0314$, which by means of (5) yields a polarization vector:

$$\mathbf{E}_t = \begin{pmatrix} 0.844 - 0.0168i \\ -0.0265 - 0.535i \end{pmatrix}.$$

The complex voltages, magnitudes, and powers then are

$$V_r = 0.434 - 4.40 \times 10^{-3}i,$$

$$|V_r| = 0.434, \quad P_r = 0.188,$$

$$V_o = -0.0192 + 4.82 \times 10^{-4}i,$$

$$|V_o| = 0.0192, \quad P_o = 3.69 \times 10^{-4}.$$

The total power P_t is calculated to be 0.312 and $\aleph$ = 0.603. These values of ϵ and τ were chosen because they correspond to ϵ_{op} and τ_{op}. The value of the figure of merit $\aleph$ at horizontal polarization (denoted as $\aleph_{HH}$) is calculated simply by expressing the HH polarization as

$$\mathbf{E}_t = \begin{pmatrix} 1 \\ 0 \end{pmatrix}.$$

Using this polarization vector the values of P_r and P_o are found to equal unity and

$$\aleph_{HH} = \frac{1}{1 + A + P_n} = 0.0168.$$

The improvement factor is computed as IF = $\aleph/\aleph_{HH}$ = 35.9. The entire $\aleph(\epsilon, \tau)$ surface is shown in Fig. 8 with the maximum labeled. The HH polarization corresponds to $\epsilon = 0$ and $\tau = 0$, which is at the center of the tilt–ellipticity plane. We can see that the peak of $\aleph$ is quite sharp and is away from the horizontal polarization—it is in fact much closer to a circular one.

6. Discussion of simulation results

We begin our discussion with Fig. 9 where four surface plots of $\aleph$ versus ellipticity ϵ and tilt τ are shown. These plots are arranged in the order of increasing incidence angle (measured from nadir) over a range of angles from 5° to 40°. The data is for X band (λ = 3.21 cm or 9.35 GHz) and corresponds to a rain rate of 45.4 mm h^{-1}, and the ocean scattering matrices are taken from calculations (Bahar and Fitzwater 1986). Note that the scale is not important here, only the relative shapes of the surfaces.

There are several features of interest in this sequence of plots. First of all, there is a well-defined peak at certain "optimal" polarizations but it moves as the angle of incidence changes. Near nadir, circular polarizations provide much better contrast but there is a trend toward linear HH polarizations at larger angles (HH corresponds to the center of the plot). One also notes that the sharpness of the peaks decreases with the increasing angle of incidence θ. This is so because the surface-to-rain return ratio A is decreasing with increasing angle making the ocean contribution less dominant. On the other hand, the sharpness of the peaks at small angles is due to the fact that $\aleph$ is maximal when the ocean contribution is nullified, which happens only at the "right" polarization, given by (13) (see appendix B for further details where it is shown that $\aleph$ behaves as the ratio P_r/P_o for small angles). At larger angles, however, this argument no longer applies, because maximum of $\aleph$ is no longer achieved when the ocean contribution is minimal.

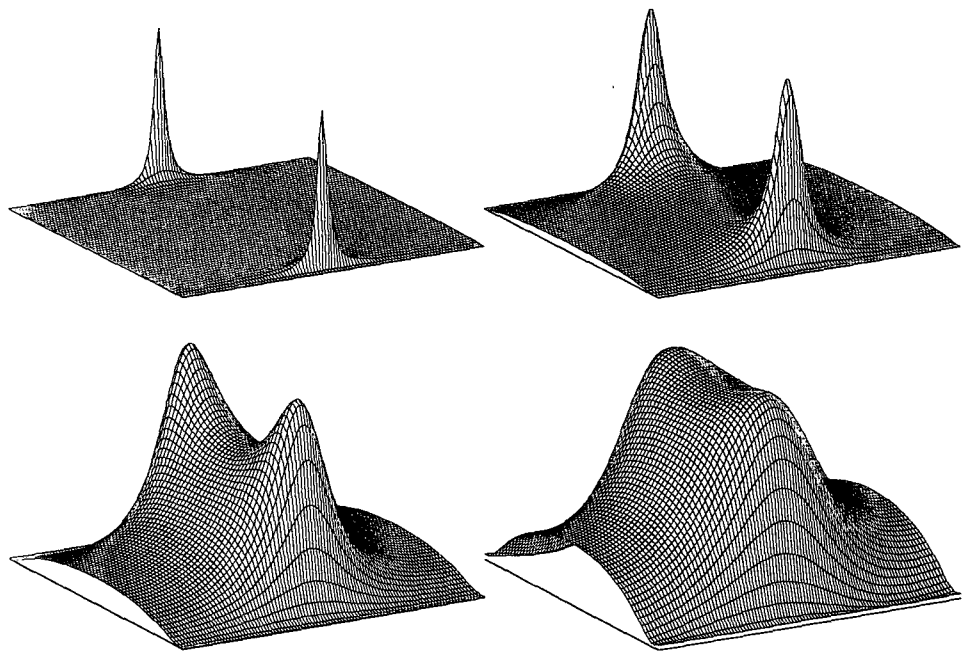

FIG. 9. The figure of merit $\aleph$ (relative strength of rain echo compared with total return) is shown as a function of ellipticity ϵ and tilt τ of the transmitted wave for incidence angles of 10°, 20°, 30°, and 40° and at a rain rate of 45.4 mm h^{-1}. The angle increases from left to right and top to bottom. The leftmost axis of each plot is the ellipticity axis (see Fig. 8). The point of this figure is to illustrate the effect of the incidence angle on the optimal ellipticity and tilt. Observe that the optimal polarization moves from circular toward linear (HH) as one looks farther away from nadir.

The sharpness of the peaks implies sensitive polarization dependence. As can be seen in the first three $\aleph$ surface plots for θ = 10°, 20°, and 30°, the maximal polarizations are well peaked. However, small deviation from ϵ_{op}, τ_{op} yields results only slightly or no better than HH. The actual improvement gained by picking the optimal polarization as opposed to the horizontal one can be characterized by the improvement factor IF [Eq. (17)]. The improvement factor (in decibels) is shown in Fig. 10 versus the angle of incidence θ with rain rate as a curve parameter. The data points in this plot represent seven sequences of nine surface plots (for seven rain rates); that is, each of the seven is similar to the one shown in Fig. 9.

There is an interesting plateau in Fig. 10 between 10° and 25° where the improvement is particularly noticeable (10–22 dB depending on the rain rate). Somewhat counterintuitive is the fact that IF is maximal for the light rain of 5 mm h^{-1} and decreases with increasing rain rate. One must remember, however, that 5 mm h^{-1} is very close to the median of the rainfall distributions, particularly in the tropical region [Simpson 1988 (p. 34 analyzes GATE data); Theon and Matsuno 1992], which makes it an important rain rate.

In Fig. 11 optimal ellipticity is shown as a function of the incidence angle with the seven curves corresponding to seven different rain rates collapsing almost entirely on a single curve. This apparent insensitivity of optimal ellipticity at X band to the rain rate is probably due to the overwhelming effect of the ocean echo in the figure of merit, particularly at near-nadir incidence. This behavior is harder to understand at greater

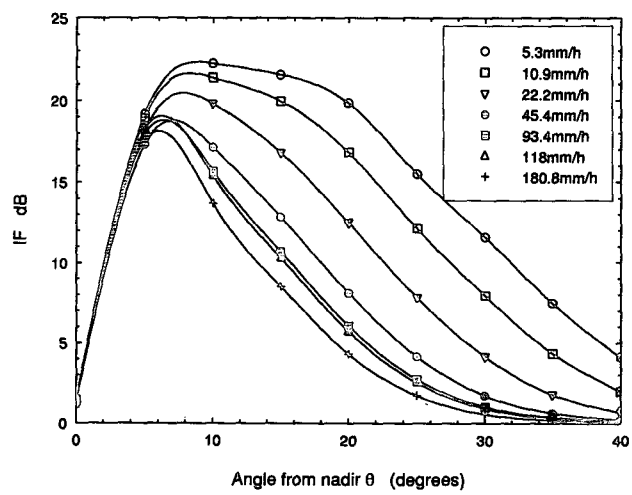

FIG. 10. Improvement factor IF (ratio of figure of merit at optimal and HH polarizations) shown as a function of incidence angle θ for several rain rates at X band. The ocean scattering matrices were taken from computations of Bahar and Fitzwater (1986). Note that cubic splines were used to connect the points so that there are some artifacts—for example, curvature between 5° and 10° data.

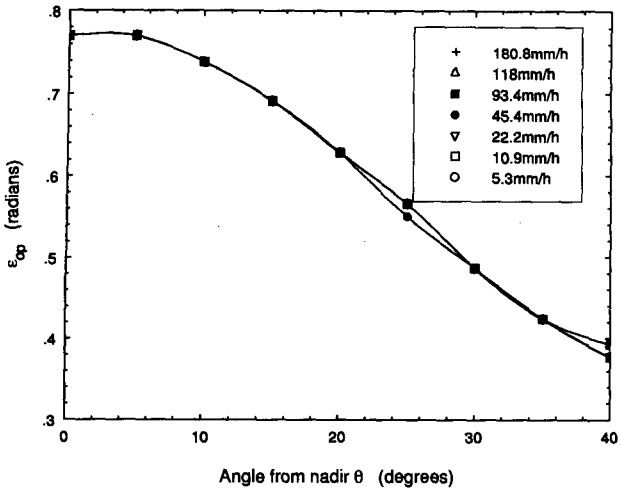

FIG. 11. The optimal ellipticity ϵ_{op} (i.e., the ellipticity that renders the figure of merit maximal) is shown as a function of incidence angle θ for various rain rates at X band. The ocean scattering matrices were taken from computations of Bahar and Fitzwater (1986). The curve appears remarkably insensitive to rain rate. This is probably due to the dominating role of ocean echo in the figure of merit. This fact makes good quality polarimetric ocean data critically important.

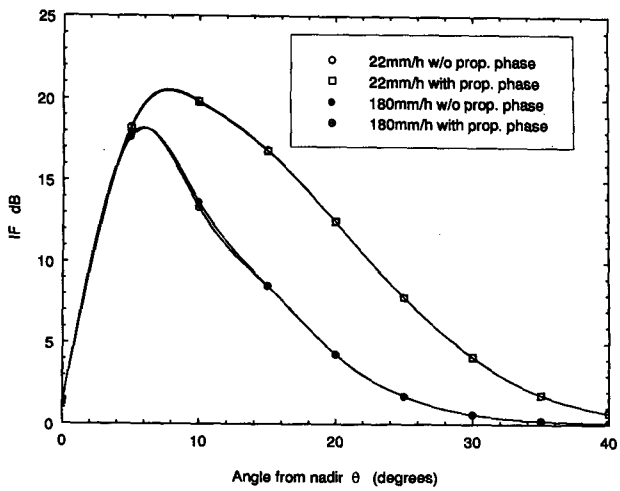

FIG. 12. Comparison of improvement factor (ratio of figure of merit at optimal and HH polarizations) curves versus incidence angle (at X band) for cases with and without rain propagation effects in the ocean matrix. The computations were performed for rain rates of 22 and 180 mm h^{-1}. Ocean data source: Bahar and Fitzwater (1986). Note that the effect of propagation phases in the ocean matrix is small.

angles where the ratio of rain and ocean echoes (A) is near unity. Angular dependence of A must also be a sensitive function of ocean roughness and is, therefore, likely to vary from one dataset to another. It is possible, in principle, to implement an adaptive technique where a scatterometer is used first to measure the roughness of the ocean surface, an appropriate curve for A is chosen next, and polarization adjusted accordingly. The optimal tilt τ_{op} is small for all rain rates and look angles, but at near nadir, incidence optimal polarizations are close to circular and the tilt is therefore poorly defined.

To examine the effects of propagation phase on the ocean scattering matrix, we have included calculations at rain rates of 22 and 180 mm h^{-1} with and without the propagation phases. At highest rain rate, propagation effects are greatest (see Fig. 5) and change the improvement factor and optimal polarization the most. Figure 12 shows the improvement factor versus incidence angle for the two rain rates with and without propagation effects included in the ocean matrix. The higher rain rate of 180 mm h^{-1} shows minor differences between the two cases while the lower rain rate shows hardly any change.

In Fig. 13 the optimal ellipticity is plotted versus incidence angle for the 180 mm h^{-1} case. The largest deviation from the case without propagation phases can be seen at 40° and is approximately 0.06 rad. The change in ϵ_{op} for the lower rain rate is negligible.

These results seem to indicate that the improvement factor is relatively insensitive to the rain propagation effects in the ocean signal. However, the optimal polarization is altered somewhat; for example, the tilt of the optimal polarization is no longer close to zero (the tilt is not defined for circular polarizations that occur close to nadir). The tilt increases at large angles due to the phases in the ocean matrix (see appendix A). In summary, it appears that inclusion of propagation effects in the ocean matrix causes no qualitative changes in most of the results.

To complete the discussion of the X-band simulation results we consider the signal-to-noise aspect of the problem. This issue is very important because $\aleph$ optimization allows rain signals to drop too low at times,

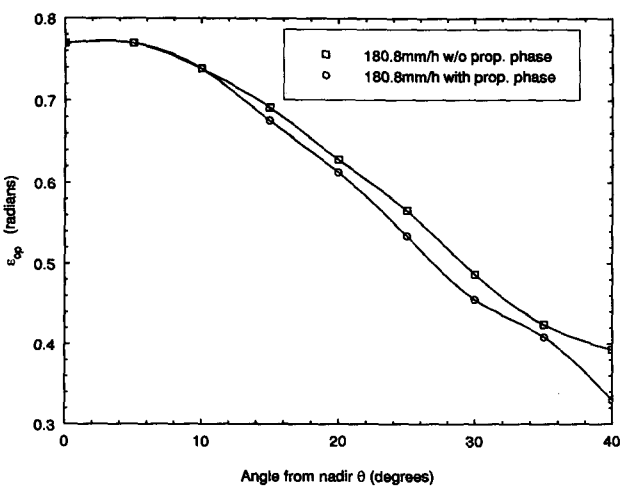

FIG. 13. Comparison of optimal ellipticity versus incidence angle curves (at X band) for cases with and without rain propagation effects in the ocean matrix. The computations were performed for rain rates of 180 mm h^{-1}. Ocean data source: Bahar and Fitzwater (1986).

particularly near nadir, because circular polarization cancels the rain signal as well as the ocean one.

The ratio of the rain return to the noise power is plotted in Fig. 14 versus the incidence angle θ for the seven rain rates, while Fig. 15 shows the improvement factor IF versus θ for three different levels of system noise at a rain rate of 5.3 mm h^{-1}.

We see from Fig. 14 that at nadir and at a 5.3 mm h^{-1} rain rate, the rain signal is 20 dB below the noise level but already by 10° it is only 10 dB below. At rain rates of 22 mm h^{-1} and higher, the ratio is close to or exceeds 0 dB at all angles beyond 10°. Also observe that the ratio exceeds 0 dB for angles greater than 20° at all rain rates.

Interpretation of these results depends critically on whether pulse averaging is available or not. If one averages over 64 or 128 pulses, then the fact that the rain signal for 5.3 mm h^{-1} is 10 dB down from the minimal detectable level (at circular polarization) implies that it can be "pulled out" from the noise. Cautious analysis of these "first-order" simulations indicates that for X band nearly circular (ϵ of 0.65–0.75) polarizations might be advantageous at incidence angles between 15° and 20°.

In Fig. 15 the system noise power P_n has been increased by increasing the system noise σ while holding the rain rate, and therefore HH, constant. The improvement factor decreases with increased P_n as expected; however, at five times the minimum noise power, which is an extremely adverse condition, polarization still gives a factor of 15-dB improvement. At these high noise levels and small rain rate, the ability of the radar to discern the rain signal is diminished. However, averaging over successive pulses might improve the situation.

Again we see that the range of angles from 10° to 25° is particularly promising in terms of the improvement that polarization agility can deliver and both Figs. 10 and 14 attest to this observation. Figure 11, on the other hand, shows within this range of viewing angles that the optimal polarization is fairly close to the circular one and is practically independent of rain rate. These observations make monostatic spaceborne X-band radar with circular polarization appear promising (and inexpensive, i.e., about the same cost as the linearly polarized one). Also observe that circular polarization is not affected by ionospheric Faraday rotation. For linear polarizations at 9 GHz the ionospheric phase shifts could be close to a radian (Allnutt 1989, p. 68).

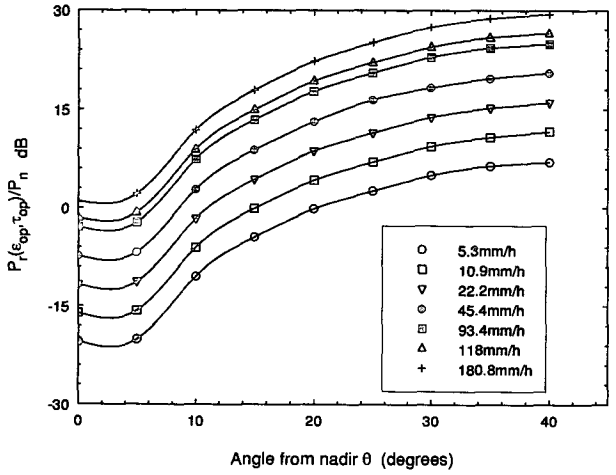

FIG. 14. Signal-to-noise ratio of rain signal at optimal polarization is shown as a function of angle of incidence θ, at X band. Ocean data source: Bahar and Fitzwater (1986).

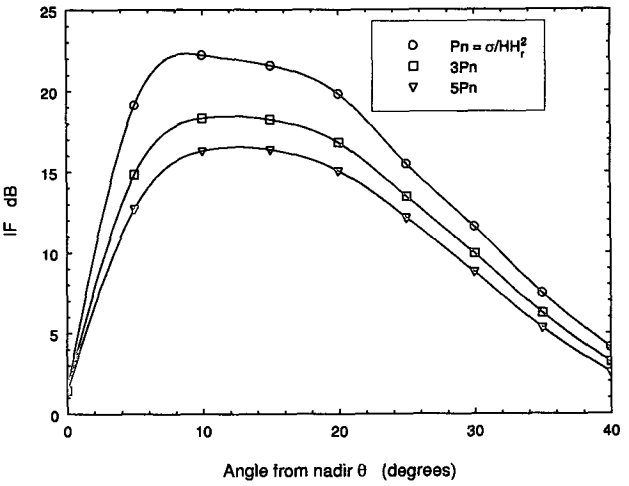

FIG. 15. Improvement factor as a function of incidence angle is shown here for a rain rate of 5.31 mm h^{-1} and for three system noise (σ) values, at X band. Ocean data source: Bahar and Fitzwater (1986). Observe decrease of the improvement factor with increasing noise, which is to be expected.

To test the sensitivity of the previous paragraph's conclusions to specific meteorological conditions we decided to repeat the calculations for both ocean and rain scattering matrices in C band (λ = 5.47 cm). As discussed in section 4, fully polarimetric data for various rain rates and ocean surfaces was virtually impossible to obtain. The ocean surface data is crucial particularly at smaller angles because the figure of merit $\aleph$ as well as the ratio X "blow up" as the ocean return approaches zero.

The only experimental data we were able to obtain was the JPL set. The JPL data does, however, include several counterintuitive features (see section 4a), and we felt that it had to be supplemented with a "well-behaved" theoretical set in order to probe a wide variety of conditions. The calculations (Fung et al. 1990) were picked for that purpose but they apply for very smooth surfaces only (see section 4a).

Let us begin the discussion of C-band results by analyzing Figs. 16 and 17 where IF versus θ (for the seven rain rates) is shown for the (Fung et al. 1990) and (Jet Propulsion Laboratory 1991) data, respectively. In Fig. 16 the improvement factor IF decreases for $\theta \geq 15°$,

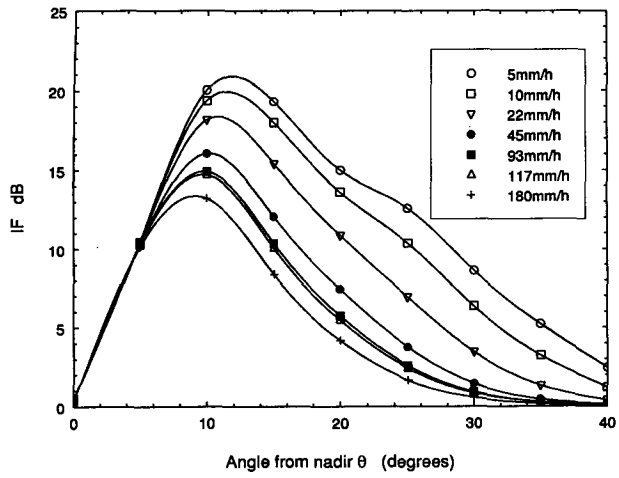

FIG. 16. Improvement factor IF (ratio of figure of merit at optimal and HH polarizations) shows as a function of incidence angle θ for several rain rates at C band. The ocean scattering matrices were taken from computations of Fung et al. (1990).

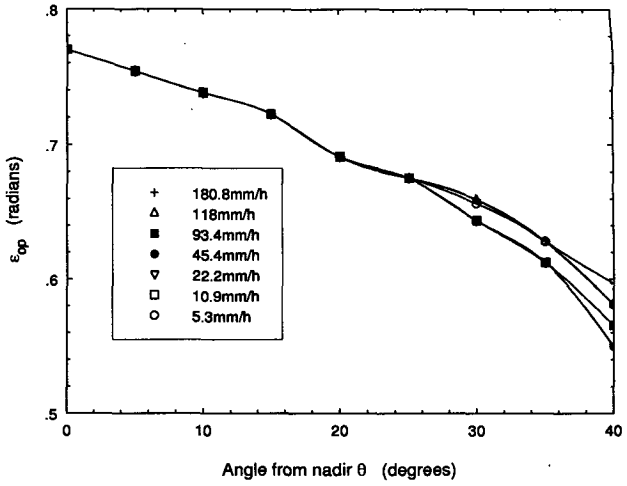

FIG. 18. The optimal ellipticity ϵ_{op} (i.e., the ellipticity that renders the figure of merit maximal) is shown as a function of incidence angle θ for various rain rates at C band. The ocean scattering matrices were taken from computations of Fung et al. (1990).

while in Fig. 17 IF decreases as θ increases for all angles. Note again that the JPL data includes only angles greater than or equal to 10°. The α versus θ curves are quite different in the two cases (see Fig. 6), and it is the dip in the JPL α versus θ curve between 20° and 30° that causes the minimum of IF for some rain rates at about 25°. Note that IF is fairly high for both datasets (Figs. 16 and 17) in the range of 10° to 20°, which is in accord with the X-band results.

All three datasets give an improvement between 5 and 20 dB in this range, but given the A dependence on θ, picking the look angle closer to 20° and the transmitted polarization near the circular one seems to be a particularly promising combination for all rain rates!

To test the last point we repeat the optimal polarization calculations for the two C-band cases also. Figures 18 and 19 give the optimal ellipticity ϵ_{op} versus θ (i.e., the ellipticity of polarization vector at which the maximum $\aleph$ occurs). While the general trends are quite different on the two graphs, numerical deviations of ϵ_{op} from the circular one ($\epsilon = \pi/4$) are rather small for angles up 30°. We again see that between 10° and 20° a circularly polarized monostatic radar would appear to perform reasonably well in both bands and for all rain rates.

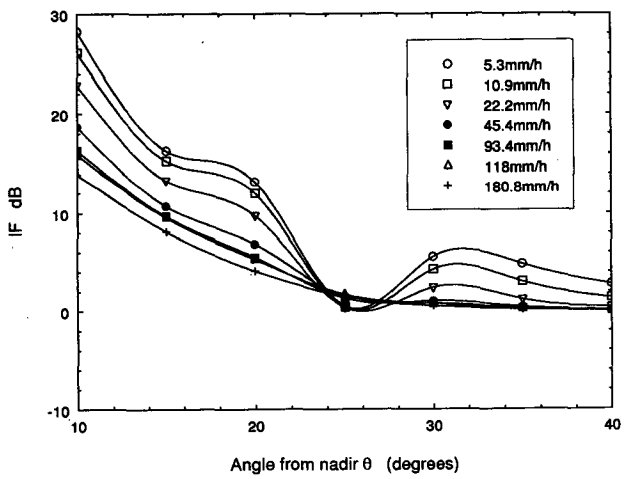

FIG. 17. Improvement factor IF (ratio of figure of merit at optimal and HH polarizations) shown as a function of incidence angle θ for several rain rates at C band. The ocean scattering matrices were taken from experimental data (Jet Propulsion Laboratory 1991). The somewhat erratic shape of these curves is probably due to the atypical behavior of the ratio of copolar returns for this dataset (see Fig. 6).

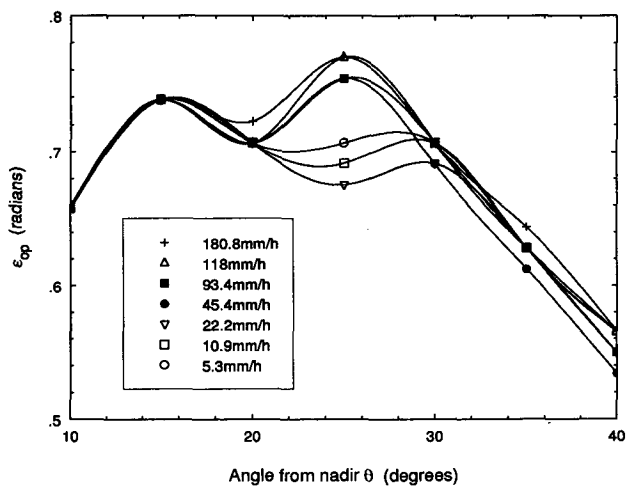

FIG. 19. The optimal ellipticity ϵ_{op} (i.e., the ellipticity that renders the figure of merit maximal) is shown as a function of incidence angle θ for various rain rates at C band. The ocean scattering matrices were taken from experimental data (Jet Propulsion Laboratory 1991).

7. Concluding remarks

We have learned several interesting lessons from this preliminary feasibility study. Most importantly, the simulation results appear encouraging. Indeed, in spite of assuming that rain and surface echoes mix throughout the entire radar resolution volume, as well as assuming no-pulse averaging, one can still pick a polarization that while almost totally canceling the ocean return keeps the hydrometeor echo detectable for a range of rain rates and look angles.

The method developed here allows one to explicitly include the detectability requirement with only a slight modification of the numerical procedure; for example, $\aleph$ can be set to zero when rain echo falls below a certain threshold. Pulse averaging can be easily incorporated as well. This can be accomplished by maximizing $\aleph$, subject to the constraint that P_r is greater than or equal to $P_n/\sqrt{N}$, where N is the number of pulses being averaged.

It must also be remembered that the mirror return (Meneghini and Kozu 1990) as well as surface return caused by the antenna sidelobes can be a serious problem and has not been considered here. However, these returns are likely to be dominated by the deviations of α from unity even more so than the ordinary surface echo (because of double scattering), and the ocean cancellation argument should still apply.

The lowest rain considered is 5.3 mm h^{-1}. This is probably not low enough, but we suspect that as one approaches drizzle rates (1 mm h^{-1}) all drops become spherical and polarimetric adjustment is then reduced to an ocean signal minimization problem (while keeping rain echo detectable). Generalizations of our method to bistatic and adaptive polarimetry are also straightforward. In any event, future studies can incorporate such extensions, but at this stage lack of high quality ocean data does not, in our opinion, warrant it. Indeed, the improvement factor as well as the figure of merit $\aleph$ are more sensitive to ocean than to rain data as detailed in appendix B. Because of this fact we feel the results presented here must be considered preliminary until more reliable and diverse polarimetric ocean data can be obtained.

The most promising range of angles for both X- and C-band cases appears to be between 10° and 25° (depending on the minimal detectable signal, rain rate, and availability of pulse averaging). The optimal polarization in this range of angles is fairly close to the circular one. These conclusions appear to be rather insensitive to the rain rate and even to the ocean surface roughness but the latter one does seem critical at very small angles or angles where α is near unity.

Furthermore, we wish to emphasize that the results described here can be obtained with a monostatic radar perhaps even at a single and fixed but elliptical transmitter–receiver polarization. Such a radar used for routine observations would seem to be as economically feasible as a linearly polarized one.

It is reasonable to expect better results when a bistatic or adaptive polarization arrangement is allowed. This is particularly so if pulse averaging is performed and more attention is given to statistical considerations affecting the minimal detectable noise figure.

Finally, we would like to note that the general "polarization contrast" method developed here is not by any means restricted to sensing precipitation over an ocean surface. For instance, in the case of a single-frequency radar such as TRMM, the surface return might provide an estimate of path-integrated attenuation. Thus, if pulse compression is not used, suppressing the surface return would be counterproductive, and one might in fact wish to maximize the surface return in the presence of high attenuation. Also, the approach may have relevance for general problems of radar and lidar meteorology—for example, hail versus rain discrimination.

Acknowledgments. One of us (JMK) would like to acknowledge NASA's support for this work given by means of the Global Change Graduate Student Fellowship. Partial support for ABK through a subcontract from the Applied Research Corporation under Grant 958437 from JPL and from a National Science Foundation Grant ATM-9116075 is gratefully acknowledged. ARJ's contribution to this study was supported under Grant 958437 from JPL in support of the NASA SIR-C program. ABK and JMK would like to thank Connie Peterman, Diane Marsh, and Jim Hoel at the Center for Experimental Computation at MTU for their help and patience with our large volumes of data.

APPENDIX A

Cancellation of Ocean Return

For the matrix of the form

$$\mathbb{S}_o = \begin{pmatrix} 1 & \delta \\ \delta & \alpha \end{pmatrix}$$

a transmitted polarization can be found such that the return from the ocean V_o can be canceled. Let us construct a polarization vector that has one complex parameter x that uniquely describes all polarizations (Kostinski and Boerner 1986):

$$\mathbb{E} = \frac{1}{(1 + |x|^2)^{1/2}} \begin{pmatrix} 1 \\ x \end{pmatrix}.$$

As x approaches zero, horizontal polarization is approached, and as x approaches ∞, $\mathbb{E}$ corresponds to vertical polarizations. Using the ocean matrix

$$\mathbb{S}_o = \begin{pmatrix} 1 & \delta \\ \delta & \alpha \end{pmatrix}$$

and the voltage equation (8), V_o can be written as a quadratic,

$$V_o = \frac{1 + 2\delta x + \alpha x^2}{1 + x^2},$$

with real coefficients δ and α.

This can be set to zero when

$$x = \rho \equiv -\frac{\delta}{\alpha} \pm \frac{(\delta^2 - \alpha)^{1/2}}{\alpha}.$$

In the special case $\delta = 0$, ρ reduces to

$$\rho = \pm i \frac{1}{\sqrt{\alpha}}.$$

The complex polarization parameter χ (Azzam and Bashara 1977) can be defined as

$$\chi \equiv \frac{E_y}{E_x} = \pm i \frac{1}{\sqrt{\alpha}},$$

which maps each polarization state onto the complex plane. For the special case $\delta = 0$, χ is a purely imaginary quantity. Thus, the optimal ellipticity and tilt are given by

$$\epsilon_{op} = \pm \tan^{-1}\left(\frac{1}{\sqrt{\alpha}}\right),$$

and $\tau_{op} = 0$ or $\pm\pi/2$ depending on $|\chi|$ being less or greater than unity, respectively. At these polarizations the ocean return is zero. The magnitude of χ depends only on α and since the JPL data for some angles gives $\alpha < 1$, τ fluctuates between 0 and $\pm\pi/2$. Note that after including the propagation phases in the ocean matrix, χ acquires a real part, and therefore, τ begins to deviate from zero.

In the general case, when off-diagonal ocean terms are included, we observe that at large angles $\tau \approx 0$. This can be justified by the fact that as θ increases, $\delta^2 - \alpha$ gets large compared to δ, and ρ acquires a large imaginary part. Thus χ is heavily imaginary and $\tau \approx 0$ at angles greater then a few degrees. At nadir, however, the optimal polarization approaches the circular one, and the tilt is poorly defined.

APPENDIX B

Small-Angle Approximations

Here we include a short discussion of the behavior of $\aleph$ and the improvement factor IF at small angles. For convenience, the definitions of both are again given here:

$$\aleph \equiv \frac{P_r}{P_r + AP_o + P_n},$$

$$\mathrm{IF} \equiv \frac{\aleph_{max}}{\aleph_{HH}}.$$

Also the definition of $\aleph_{HH}$ is

$$\aleph_{HH} = \frac{1}{1 + A + P_n}.$$

At small angles the ratio of ocean to rain returns A is very large compared to unity and the nondimensional powers P_r, P_o, and P_n. Thus, $\aleph$ and $\aleph_{HH}$ can be written as

$$\aleph = \frac{P_r}{AP_o}$$

and

$$\aleph_{HH} = \frac{1}{A}.$$

The maximum of aleph $\aleph_{max}$ is achieved only by minimizing the ocean return, and the improvement factor reduces to

$$\mathrm{IF} = \frac{P_r}{P_o},$$

where P_r and P_o are calculated at the polarization, which minimizes P_o. This approximation holds numerically in our calculations for all rain rates and for $\theta = 0°$.

APPENDIX C

Justification of the Typical Scattering Matrix Concept

As was pointed out in section 4, both rain and ocean scattering matrices fluctuate in time and space. We nevertheless conjecture that the corresponding random matrix sequences have a "typical" structure. To demonstrate the plausibility of this conjecture consider a sequence of random matrices of the form

$$\mathbf{S} = \lambda(t)\begin{pmatrix} \mathrm{HH}e^{i\delta_{HH}} & \mathrm{HV}e^{i\delta_{HV}} \\ \mathrm{VH}e^{i\delta_{VH}} & \mathrm{VV}e^{i\delta_{VV}} \end{pmatrix},$$

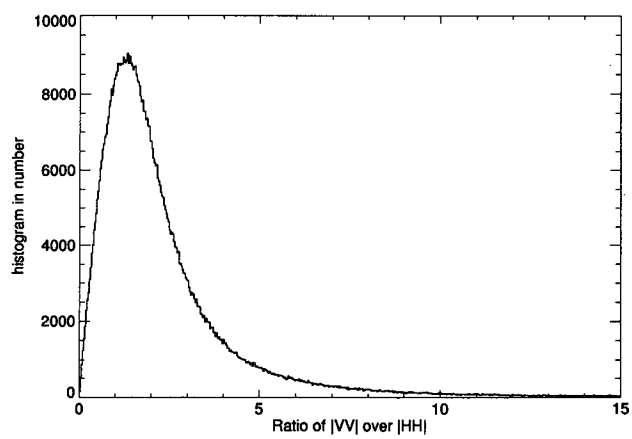

FIG. C1. Histogram of α (ratio of copolar returns) for the ocean surface. Several rows of a 1024-pixel × 768-pixel JPL SAR image were used to obtain this histogram (J. van Zyl 1992, personal communication).

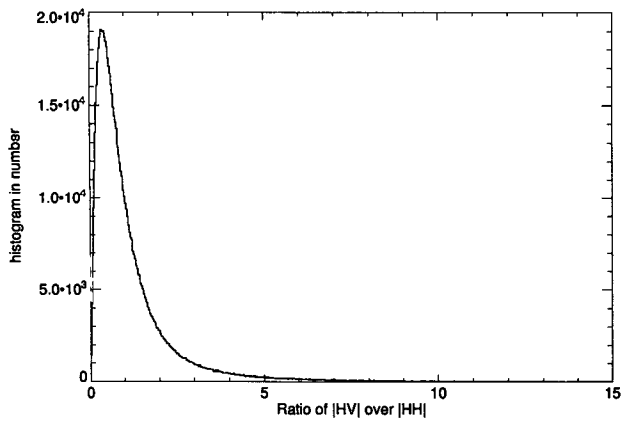

FIG. C2. Histogram of δ (ratio of cross-polar returns) for ocean surface. Several rows of a 1024-pixel × 768-pixel JPL SAR image were used to obtain this histogram (J. van Zyl 1992, personal communication).

where $\lambda(t)$ is a random function and the scattering matrix is deterministic. Does the sequence correspond to a random target? Yes and no. Every element measured separately would appear entirely random (because of the random multiplier) but the elements are perfectly correlated. In most practical situations one encounters the general partially polarized case. To justify our use of the "typical" scattering matrix, histograms of α and δ are presented in Figs. C1 and C2. These histograms were obtained from a JPL SAR ocean surface dataset (only several rows of the image were taken to preserve the same incidence angle). Observe that the peaks are relatively sharp indicating a structured sequence of matrices in spite of Rayleigh-like intensity fluctuations from pixel to pixel.

Note added in proof: Two important improvements have emerged from several discussions held during the recent 26th Radar Meteorology Conference in Norman, Oklahoma both dealing with the proper choice of A in (13). One should set the *effective* A to smaller values because of the calming influence of raindrops on the sea (D. Atlas 1993, private communication), and to multiply it by a system-dependent coefficient describing the relative intensity of sidelobes or range precursors.

REFERENCES

Allnutt, J. E., 1989: *Satellite to Ground Radiowave Propagation.* Peregrinus, 68 pp.

Azzam, R. M. A., and N. M. Bashara, 1977: *Ellipsometry and Polarized Light.* North-Holland, 539 pp.

Bahar, E., M. A. Fitzwater, 1986: Scattering cross sections for composite rough surfaces using the unified full wave approach. *IEEE Trans. Antennas Propag.*, **32**, 730–734.

Beard, K. V., D. B. Johnson, and A. R. Jameson, 1983: Collisional forcing of raindrop oscillation. *J. Atmos. Sci.*, **44**, 448–454.

Bohren, C., and D. Huffman, 1983: *Absorption and Scattering of Light by Small Particles.* Wiley and Sons, 530 pp.

Born, M., and E. Wolf, 1980: *Principles of Optics.* 6th ed. Pergamon, 808 pp.

Bringi, V. N., and A. Hendry, 1990: Technology of polarization diversity radars for meteorology. *Radar Meteorology,* D. Atlas, Ed., Amer. Meteor. Soc., 153–190.

Chuang, D., and K. V. Beard, 1991: A new model for the equilibrium shapes of rain drops. *J. Atmos. Sci.*, **44**, 1509–1524.

Curlander, J. C., and R. N. McDonough, 1991: *Synthetic Aperture Radar: Systems and Signal Processing.* Wiley and Sons, 647 pp.

Daley, J. C., 1973: Wind dependence of radar sea return. *J. Geophys. Res.*, **78**, 730–734.

Doviak, R. J., and D. S. Zrnić, 1984: *Doppler Radar and Weather Observations.* Academic Press, 458 pp.

Fung, A. K., A. J. Blanchard, and M. F. Chen, 1990: Polarization properties in random surface scattering. *Polarimetric Remote Sensing,* J. A. Kong, Ed., Elsevier, 520 pp.

Im, K. E., D. Atlas, 1988: The estimation of precipitation intensity in the presence of surface backscatter and the converse using a spaceborne radar. *Tropical Rainfall Measurements,* J. S. Theon, and N. Fugono, Eds., A. Deepak, 221–228.

Ishimaru, A., 1991: *Electromagnetic Wave Propagation, Radiation, and Scattering.* Academic Press, 637 pp.

Jameson, A. R., 1987: Relations among linear and circular polarization parameters measured in canted hydrometeors. *J. Atmos. Oceanic Technol.*, **4**, 634–645.

——, 1991: A comparison of microwave techniques for measuring rainfall. *J. Appl. Meteor.*, **30**, 32–53.

Jet Propulsion Laboratory, 1991: *SIR-C/X-SAR Calibration/Validation Working Group Meeting.* Oberpfaffenhofen, Germany, 20 pp. [Available from Tony Freeman, Mail Stop 300-233 JPL, Pasadena, CA 91109.]

Kostinski, A., and W-M. Boerner, 1986: On foundations of radar polarimetry. *IEEE Trans. Antennas Propag.*, **34**, 1395–1404.

——, and ——, 1987: Polarimetric contrast optimization. *IEEE Trans. Antennas Propag.*, **35**, 988–990.

——, B. James, and W-M. Boerner, 1988: Polarimetric matched filter for coherent imaging. *Can. J. Phys.*, **66**, 871–877.

Long, M. W., 1975: *Radar Reflectivity of Land and Sea.* Lexington Books, 366 pp.

Meneghini, R., and T. Kozu, 1990: *Spaceborne Weather Radar.* Artech House, 32 pp.

Okamoto, K., T. Kozu, K. Nakamura, and T. Ihara, 1988: Tropical Rainfall Measuring Mission rain radar. *Tropical Rainfall Measurements,* J. S. Theon, and Fugono, Eds., A. Deepak, 217 pp.

Pruppacher, H. R., and K. V. Beard, 1970: A wind tunnel investigation of the internal circulation and shape of water drops falling at terminal velocity in air. *Quart. J. Roy. Meteor. Soc.*, **96**, 247–256.

Sekhon, R. S., and R. C. Srivastava, 1971: Doppler radar observations of drop-size distributions in a thunderstorm. *J. Atmos. Sci.*, **28**, 983–994.

Simpson, J., 1988: *Tropical Rainfall Measuring Mission (TRMM): Report of The Science Steering Group.* NASA, Goddard Space Flight Center, Greenbelt, MD, 94 pp.

——, R. F. Adler, and G. R. North, 1988: A proposed satellite Tropical Rainfall Measuring Mission (TRMM). *Bull. Amer. Meteor. Soc.*, **69**, 278–295.

Theon, J. S., and T. Matsuno, Eds., 1992: *The Global Role of Tropical Rainfall.* A. Deepak, 280 pp.

Ulaby, F. T., and C. Elachi, 1990: *Radar Polarimetry for Geoscience Applications.* Artech House, 364 pp.

Warner, C., and A. Hizal, 1976: Scattering and depolarization of microwaves by spheroidal raindrops. *Radio Sci.*, **11**, 921–930.

Zebker, H. A., J. van Zyl, and D. N. Held, 1987: Imaging radar polarimetry from wave synthesis. *J. Geophys. Res.*, **92**, 683–701.